

Research Article

Narrow-Band Radio Propagation Prediction Based on a Highly Accurate Three-Dimensional Railway Environment Model

Jinhan Li ^{1,2}, Lihai Liu,¹ and Ke Guan²

¹China Railway Siyuan Survey and Design Group Co. Ltd., Wuhan, 430061 Hubei, China

²Beijing Jiaotong University, Beijing 100091, China

Correspondence should be addressed to Jinhan Li; 007350@crfsdi.com

Received 19 December 2021; Revised 17 February 2022; Accepted 3 March 2022; Published 18 March 2022

Academic Editor: Luis Castedo

Copyright © 2022 Jinhan Li et al. This is an open access article distributed under the Creative Commons Attribution License, which permits unrestricted use, distribution, and reproduction in any medium, provided the original work is properly cited.

In this paper, radio propagation predictions were performed by a self-developed ray tracing simulator based on highly accurate three-dimensional (3D) environment models obtained by oblique aerial photography (OAP). In order to support ray tracing computations, the highly complex environment models were managed by three steps, including model separation, electromagnetic parameter assignment, and model lightweighting. Simulations and real-world experiments were conducted to test the proposed method. The results show that the root mean square errors (RMSE) in the predicted received signal strength curves were achieved 4 dB with comparably low computational complexity in the selected railway scenarios.

1. Introduction

Nowadays, the Global System for Mobile Communications-Railway (GSM-R) networks in China mainly transmit the train-to-trackside safety-related information for China Train Control System Level 3 (CTCS-3), which makes the wireless communication networks vital for high-speed railway controlling [1]. During the railway wireless network design, it is a basic step to locate the communication base stations (BS). If the network planning is conducted based on inaccurate radio propagation prediction results, it is highly potential that the deployment of BSs is not optimized and the telecom infrastructure needs to modify during constructions, which will surely add to the cost. Since the costs of the facilities supporting the BSs, including the antenna towers, backhaul equipment, communication cables, electric power supply, and housing, are much higher than the expense of the wireless system devices, the BS site locations affect not only the quality of the railway wireless communication networks but also the overall investment of the railway constructions. As a result, accurate radio propagation predictions are significant in railway wireless system design [2, 3]. The GSM-R downlink frequency band is 930-

934 MHz in China. The existing channel models for radio propagation prediction in this specific band are mainly classified into two categories: empirical channel models and deterministic channel models. Empirical channel models, such as the Hata-Okumura model [4, 5], the Stanford University Interim (SUI) model [6], and the Cost 231 model [7] are widely used owing to their high execution speed. However, the empirical channel models are usually inaccurate before measurement-based model corrections [8, 9]. Moreover, even if the model corrections are performed, the reliance on the measurements in the selected environment makes the empirical channel models less reliable when the environment changes. In order to increase the robustness and accuracy of the radio propagation predictions, deterministic channel models are developed [10–12]. By literally computing different radio propagation factors, the deterministic channel models obtain radio propagation prediction results with higher accuracy [13]. Among the deterministic channel models, ray tracing is a widely accepted tool. Ray tracing is a three-dimensional (3D) ray-optic technique computing the influence of multiple environmental factors that contribute to the signal propagation processes [14]. Direct, transmitted, reflected, and

diffracted electromagnetic fields propagating in the environment are coherently summed to simulate the real-world radio propagation. With the fast development of computer CPUs and 3D reconnaissance maps, ray tracing has already become a vital tool in wireless communication system design [15]. Ray tracing is a powerful tool in accurately describing multipath propagation, especially in complex railway scenarios. For high-speed railways, it is required to reduce the bumpiness and ensure safe operation for high-speed trains. As a result, characteristic railway environments, such as cuttings, tunnels, flyovers, and viaducts, are widely implemented in railway constructions to straighten the track, which put together may occupy over 70% of the whole railway line when the line frequently encounters obstructions or waters. The specificity of railway scenarios adds to the difficulty in network planning. Over the past decades, efforts had been made on accurately characterizing the propagation models in those specific railway environments using ray tracing [16–19]. Commercial tools like CloudRT [15], Winprop, Ranplan, and EDX were also developed to support railway scenarios. Most existing ray tracing methods calculate the radio propagation based on digital elevation model (DEM) or manual 3D modeling. The DEM describes the natural terrain in high resolution, but it is not able to fully present the railway constructions and the surrounding buildings in the environment. To make reasonable environment models, the constructions should be manually added to the 3D environment model, thus causing uncertainty to the simulations. Though the 3D environment models are imperfect, it should be emphasized that ray tracing still performs much more accurate radio propagation prediction than the empirical channel models. To further improve the performance of ray tracing and achieve highly accurate radio propagation predictions, realistic 3D environment descriptions are needed. Light Detection and Ranging (LiDAR) and Oblique Aerial Photography (OAP) are currently two representative 3D modeling technologies that are used to obtain large-scale open-area 3D environment models in high efficiency. LiDAR obtains high precision point clouds in occlusion areas, which describes the natural terrain efficiently [20]. However, the problem with LiDAR is that it is costly to fully present railway constructions and the texture of the environment models should be obtained by other technology so that the model can be applied to ray tracing. In order to produce environment models which are highly consistent with the realistic railway environments, OAP is used in this paper. OAP is a highly precise realistic 3D model restoring technology, which was widely used for producing 3D building textures over the last decades [21, 22]. With the development of computer technology and unmanned aerial vehicles (UAV), OAP attracts massive attention in geological surveys [23]. OAP obtains aerial images from different vertical and oblique angles via oblique photography platforms. Most commercial oblique photography platforms are of the “1 + 4” system structure, where one vertical and four oblique cameras are integrated on a single UAV platform. By implementing the inertial naviga-

tion system, the obtained high-resolution aerial images are arranged with their corresponding geographic locations [24, 25]. After image matching and 3D modeling, the obtained images are put into a consistent coordinate system to produce highly realistic 3D environment models. OAP obtains 3D environment models with high accuracy, which is promising of supporting highly accurate radio propagation predictions in railway scenarios. However, the challenge is that large-scale OAP environment models produced by high-resolution aerial images contain large amounts of data, which result in excessive computational complexity when performing ray tracing computations [26]. In this paper, we proposed a method to manage the OAP environment models before implementing them in a self-developed ray tracing simulator. We took advantage of OAP to accurately establish the environment models and exported them to light-weighted environment models. The proposed method was performed in two typical railway scenarios and propagation prediction results were obtained. The results show that a 4dB root mean square error (RMSE) was achieved with comparably low computational complexity.

The rest of this paper is organized as follows. Section 2 presents the simulation methods including the ray tracing simulator and environment model management. Section 3 describes and discusses the comparative experiment results of the ray tracing simulation and the field experiment. Finally, Section 4 makes conclusions on the modeling and simulation processes.

2. Materials and Methods

2.1. Ray Tracing Simulator. In order to make accurate radio propagation predictions in high-speed railway scenarios, a ray tracing simulator was developed. The existing schemes for ray tracing include the shooting and bouncing rays (SBR) method [27] and the image method (IM) [28]. Since the railway scenarios are usually distributed on a large physical scale and the radio propagation along the railway track is the primary consideration for most railway applications, only the propagation paths received by the selected observation points are necessarily considered. Therefore, we adopted the IM scheme for the ray tracing simulator to link each observation point to their corresponding source signal before calculating the radio propagation concerning the facets and edges of the obstacles in the environment model. The received power for each communication link at the observation point coherently sums up all multipath components and can be expressed in [15]

$$P(r, \theta, \varphi) = \frac{\lambda^2}{8\pi\eta_0} \left| \sum_{k=1}^{N_{\text{rays}}} E_i(\theta_i, \varphi_i) \cdot \sqrt{G(\theta_i, \varphi_i)} \right|^2, \quad (1)$$

where $G(\theta_i, \varphi_i)$ is the receiving antenna gain, λ is the radio working wavelength, η_0 is the characteristic impedance of the vacuum, θ_i and φ_i are the arrival angles of the ray i to the observation point at E_i which is the associated receiving

electric field. The receiving electric field at the observation point (O_s) is calculated using [15]

$$E_i(\theta_i, \varphi_i) = \begin{bmatrix} E_{\theta_i}(O_s) \\ E_{\varphi_i}(O_s) \end{bmatrix} = \begin{bmatrix} T_{\theta_i} \\ T_{\varphi_i} \end{bmatrix} \cdot \sqrt{\frac{\eta_0 P_r G_M}{2\pi}} \begin{bmatrix} E_{\theta_i}(\theta_s, \varphi_s) \\ E_{\varphi_i}(\theta_s, \varphi_s) \end{bmatrix} \frac{\exp(-jkr)}{r}. \quad (2)$$

The electric field is in the form of the matrix considering different polarization components of the transmitting antenna, where P_r is the radiation power of the transmitting antenna, G_M is the transmitting antenna gain, r is the radiated distance between the transmitting antenna and the observation point, $E_{\theta_i}(\theta_s, \varphi_s)$ and $E_{\varphi_i}(\theta_s, \varphi_s)$ are the vertical and horizontal components of the normalized antenna patterns of the transmitting antenna, and T_{θ_i} and T_{φ_i} represent the propagation path loss caused by the multipath components in the two corresponding polarization directions.

The multipath components include the direct, transmitted, reflected, and diffracted field components with respect to the obstacles in the environment model. For the direct, transmitted, and reflected field components, the ray tracing algorithm went through every triangular facet in the 3D environment model to find the propagation paths before calculating the path loss, implementing Fresnel's equation when necessary. Meanwhile, for the diffracted field components, each of the edges in the 3D environment model was tested using Uniform Theory of Diffraction (UTD) [15]. Because the algorithm computational complexity increases exponentially when there are higher-order reflections and diffractions, which seldom occur in wide-open scenarios, we consider only the first and second orders of reflected and diffracted components in the simulator.

Before conducting the simulations, the antenna patterns for both transmitting and receiving antennas were modeled, which are demonstrated in Figure 1. The 3D antenna pattern was obtained by interpolating the 2D patterns. The transmitting antenna was a directional dual-polarization planar antenna (YX0809X6517-DT0, Dongzhou, China) with 17 dBi gain and 65° horizontal and 9° vertical beamwidth. Meanwhile, the receiving antenna was a shark fin antenna (84002818, HUBER+SUHNER, German) located at the train rooftop. The simulation iteratively traces the rays starting from the transmitting antenna to the receiving antenna to obtain the radio propagation simulation results. The antenna gains of the propagation rays at the transmitting or receiving antennas were determined by their corresponding azimuth and elevation angles with respect to the antenna patterns.

2.2. 3D Environment Model Management. Ray tracing simulations were performed in realistic railway environments along the Zhangjiajie-Jishou-Huaihua (ZJH) high-speed railway. We built realistic 3D railway environment models using OAP. During the modeling process, the aerial images were obtained by commercial OAP devices (DG3 Pro,

Rainpoo, China) and processed to highly accurate 3D railway environment models using the software ContextCapture. Figures 2(a)–2(c) present the environment models of the three selected railway scenarios, respectively. The models for all scenarios were reconstructed by 5 cm resolution aerial images. Figure 2(a) shows the OAP environment model of scenario 1, which is a typical wide-open railway district with an area of 400 × 1200 m². Typical elements for wide-open railway sections, such as viaduct, cuttings, and tunnel entrances, were found in this specified railway area. Figure 2(b) shows the OAP environment model of scenario 2, which is a railway traffic junction area linking to the Huaihua South railway station in Hunan Province in China with an area of 500 × 2600 m². The surrounding environment in scenario 2 is more complex than that in scenario 1 because of the urban structures and the overpassed railway tracks. Figure 2(c) shows the OAP environment model of scenario 3, which is a valley area with an area of 400 × 2600 m². The bending railway track makes the radio propagation mostly obstructed by the surrounding terrain, which makes a good NLOS (non-line-of-sight) situation for railway wireless communications.

After we obtained the original OAP 3D railway environment models, the models were managed to meet the demands of the ray tracing simulator in three steps, which were the model separation, electromagnetic parameters assignment, and model lightweighting.

First of all, we separated different environment model elements into different submodels from the OAP environment model. Specifically, all environment elements were classified into six categories: vegetation, concrete, water, soil, metal, and cutting slopes. Among the six categories of elements, the vegetation elements contained the vegetated areas including forests, lawns, and farmland. The concrete elements covered most of the artificial constructions, including the viaduct, surrounding buildings, tunnel entrances, and solid grounds. The water elements included all ponds, streams, and rivers. Meanwhile, all bare ground areas were classified into soil elements and all metal-made structures were classified into metal elements. There was a special case for cutting slopes since the cuttings along the railways contributed massively to the ray tracing simulation results and were often combined material covered with bushes. In addition to the submodel separations, we also separated the artificial constructions from the natural terrain area since the artificial constructions along the railway tracks are usually close to the receiving antennas on the operating railway train and have more influence on the radio propagation. The above-mentioned model separations were conducted manually with the OAP 3D modeling software DpModeler (Wuhan Tianjihang Information Technology Co., Ltd., Wuhan, China).

After we finished the environment model separation, the electromagnetic parameters were assigned to the 3D environment model. To differentiate all six categories of elements in the 3D environment model, different colors, such as green, grey, baby blue, brown, red, and navy blue, were implemented to represent the vegetation, concrete, water, soil, metal, and cutting slope elements,

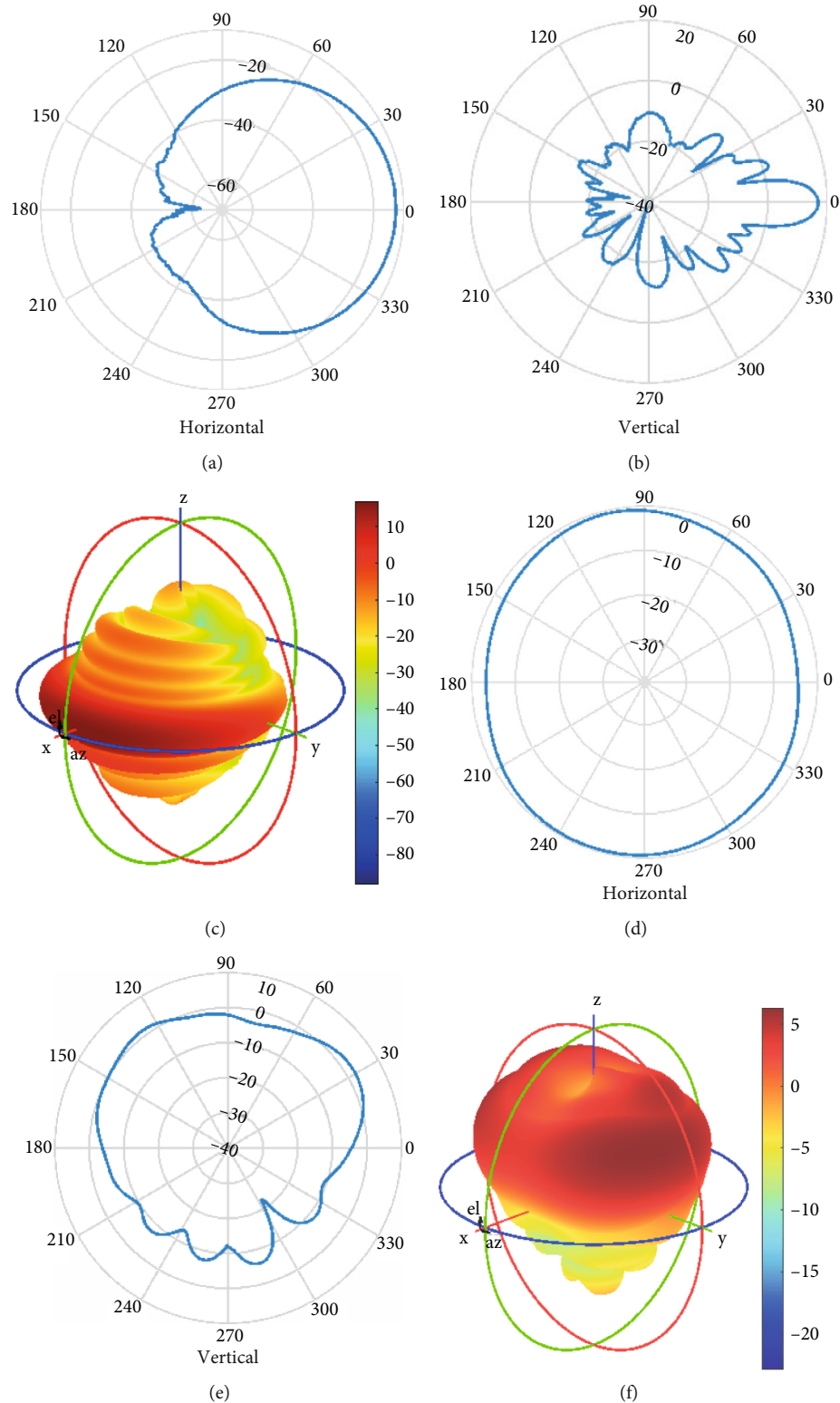


FIGURE 1: Diagrams of the horizontal and vertical antenna patterns with their interpolated 3D patterns: (a) horizontal pattern for the transmitting antenna; (b) vertical pattern for the transmitting antenna; (c) 3D pattern for the transmitting antenna; (d) horizontal pattern for the receiving antenna; (e) vertical pattern for the receiving antenna; (f) 3D pattern for the receiving antenna.

respectively. Corresponding electromagnetic parameters were linked to the element colors and the parameters were assigned to the corresponding triangular facets in the 3D

environment model in this way. The electromagnetic parameters operating in 930 MHz radiofrequency are listed in Table 1 [29–31].

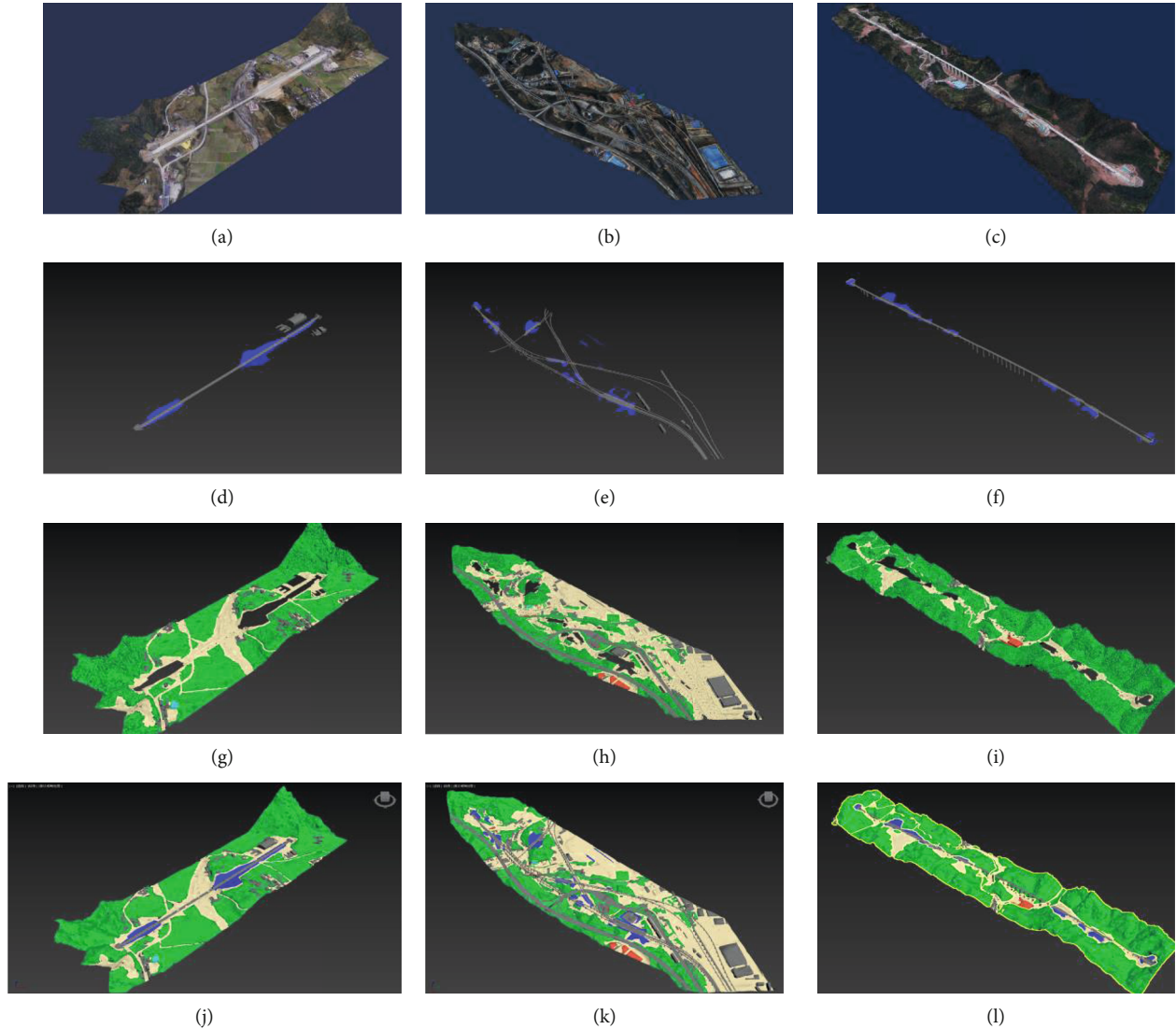


FIGURE 2: Railway 3D environment models during the model managements: (a) original OAP scenario 1 environment model with an area of $400 \times 1200 \text{ m}^2$ and over 11 M triangular facets; (b) original OAP scenario 2 environment model with an area of $500 \times 2600 \text{ m}^2$ and over 74 M triangular facets; (c) original OAP scenario 3 environment model with an area of $400 \times 2600 \text{ m}^2$ and over 45 M triangular facets; (d) the class A structure in scenario 1; (e) the class A structure in scenario 2; (f) the class A structure in scenario 3; (g) the class B structure in scenario 1; (h) the class B structure in scenario 2; (i) the class B structure in scenario 3; (j) the light-weighted scenario 1 environment model with 20k triangular facets; (k) The light-weighted scenario 2 environment model with 84k triangular facets; (l) the light-weighted scenario 3 environment model with 53k triangular facets.

TABLE 1: Electromagnetic parameters of the objects in the railway environment.

Objects	Complex permittivity
Vegetation	$18.17-j6.66$
Concrete	$5.31-j0.59$
Water	$78.81-j3.75$
Soil	$6.15-j0.64$
Metal	$1-j1.93 \times 10^8$
Cutting slopes	$8.09-j1.51$

At last, the environment models were light-weighted before being implemented in the ray tracing simulator. The model lightweighting aimed to reduce the data volume of the environment models and decrease the computational complexity while maintaining the high prediction accuracy of the simulations. The model lightweighting was performed using the ProOptimizer tool in the software 3dsmax (Autodesk, California, USA). The amounts of 3D triangular facets in the original environment models were over 11 million for scenario 1 (Figure 2(a)), 74 million for scenario 2 (Figure 2(b)), and 45 million for scenario 3 (Figure 2(c)), respectively. In this paper, we used different strategies for different submodels. Specifically, artificial constructions, such as cutting slopes, viaducts, tunnel entrances, and

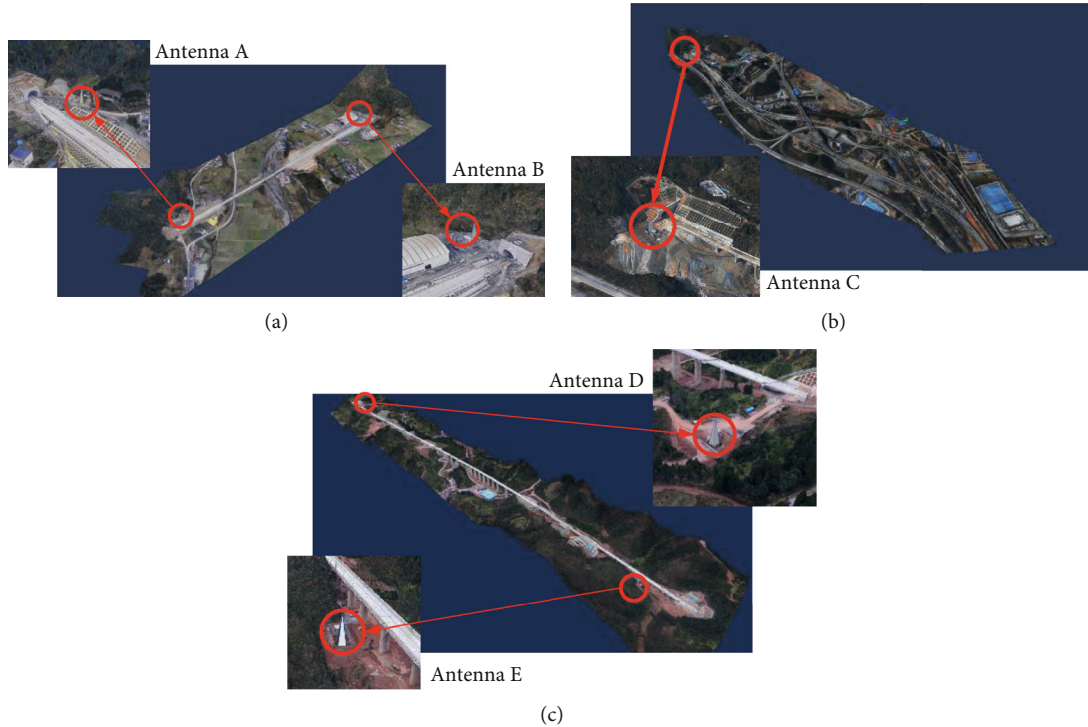


FIGURE 3: The antenna location on the 3D environment model. (a) Antenna A and antenna B in scenario 1; (b) antenna C in scenario 2; (c) antenna D and antenna E in scenario 3.

buildings beside the railway track, were considered to have the most influence on the simulation results and were classified as the class A elements (Figures 2(d)–2(f)), while the rest of the submodel in the environment model, including all surrounding vegetation, soil, and water elements as well as the remaining concrete and metal elements, were considered contributing lighter to the simulation results and were classified as the class B elements (Figures 2(g)–2(i)). During the model lightweighting, the class B elements remained only 0.1% of the model vertices, while the class A elements experienced a relatively lower lightweighting level and 1% of the model vertices remained. Figures 2(j)–2(l) demonstrated the simplified environment models. The overall numbers of triangular facets in the three environment models were reduced to 20k, 84k, and 53k, respectively.

Apart from the 3D environment models for simulation, accurately locating the transmitting antennas is also an advantage of implementing highly accurate 3D railway environment models. According to the GSM-R system design documents along the ZJH high-speed railway, the transmitting antennas in all selected scenarios are shown in Figure 3. Figure 3(a) depicts the location of the transmitting antennas in scenario 1. Antenna A and antenna B were located at the two opposite tunnel entrances. Meanwhile, the electromagnetic environment in scenario 2 is much more complex compared with that in scenario 1; hence, we discussed only the railway area before entering the railway station to simplify the simulation processes and only antenna C was concerned in this area (Figure 3(b)). Figure 3(c) shows the location of the transmitting antennas in scenario 3. Antenna D was located 74 m away from the railway track at the foot

TABLE 2: Transmitting antenna parameters.

Antenna	Tower height	Radiation power
A	20 m	34 dBm
B	20 m	33 dBm
C	30 m	38 dBm
D	40 m	31 dBm
E	50 m	34 dBm

of the earth mound beside the tunnel entrance. Antenna E was located close to the railway track at the opposite end of the district. All the antenna parameters are listed in Table 2.

3. Results and Discussion

3.1. Field Experiment. In order to obtain the real-world radio propagation in the two selected railway scenarios, field experiments were conducted. The received signal strength indicator (RSSI) curves along the railway track were obtained by conducting measurements on operating railway trains. Figure 4 demonstrates the field test environment. The transmitting antenna was installed on the installation platform on the BS tower beside the railway track (Figure 4(a)), and the receiving antenna was the shark fin antenna located at the train rooftop (Figure 4(b)).

The RSSI curves along the railway tracks were obtained by the downlink received signal levels (RXLev) exported from the Abis interface of the GSM-R communication



FIGURE 4: Pictures of the field test environment: (a) the transmitting antenna on the installation platform on the communication base station towers along the railway; (b) the shark fin antenna located at the train rooftop.

system. According to the GSM-R standards, the RXLev shall be the averaged received signal level measurement samples in dBm within the reporting period of length one SACCH multiframe (480 ms) [32]. The values of RSSI vary between -110 dBm and -47 dBm, and it is reported -47 dBm when excessive signal power was detected. Figures 5(a)–5(c) depict the RSSI curve results in contrast to the system design documents in scenario 1, scenario 2, and scenario 3, respectively. The figures show that the RSSI curves topped at -47 dBm in the near-field areas in all scenarios.

In compliance with the CTCS-3 standards for the ZJH high-speed railway, coverage of interleaved stations is demanded in the GSM-R wireless system design. As a result, all scenarios are covered with two sets of transmitting systems. Scenario 1 is an intercell handover area with the two remote unit (RU) devices belonging to different cells; hence, we resolved the RSSI curves for each of the transmitting antennas, while scenario 2 performs single-sided wireless coverage with the RU device acting in an active-standby scheme using a single transmitting antenna (antenna C). Scenario 3 is also covered with two sets of transmitting systems. However, the RU devices supporting the two antennas share the same BTS and the transmitted frequency from both antennas are the same. As a result, the receiving antenna is not able to distinguish the downlink signal from each of the two transmitting antennas and the received signal was a compound signal from both two signal sources. All field experiment results shown in Figure 5 were used for verifying the ray tracing simulation results.

3.2. Comparative Results. Radio propagation predictions implementing ray tracing were performed in all selected scenarios. Figure 6 demonstrates the comparisons between the simulation results and the experimental results. The observation points in the simulation were all chosen as 1 m evenly spaced points which were 4.5 m above the railway tracks. The height of the observation point was chosen for the reason that the shark fin antennas on the train rooftop are usually considered about 4.5 m above the railway track. Since the altitude of the railway track along a single railway line is not completely flat, the observation points were set strictly matching the railway track altitudes but not on the same 3D plane. The field test measurement results in all scenarios were obtained with the train operating at a speed about 120 km/h. So in a SACCH multiframe period (480 ms), the

train rooftop receiving antenna is about to move 16 m distance. To physically match the simulation results with the obtained measurement results exported from the GSM-R Abis interface, we averaged every 16 adjacent observation points in the simulation.

In scenario 1 and scenario 2, the three antennas in the two scenarios were simulated separately. In Figure 6(a), the received radio signal for antenna 1 was dominated by the direct and first-order reflected field components because of the comparably simple railway scenario with no obstructions. Specifically, the reflections were mainly caused by the cutting slopes beside the railway track. Antenna 2 was also in scenario 1, which was located at the opposite side of the area against to antenna 1. In this situation, there was a trackside building in front of the BS tower. Although the building was not tall enough to obstruct the direct rays, it was located within the Fresnel zone of the transmitting antenna, hence causing some diffraction. As a result, the RSSI curve in Figure 6(b) shows some fluctuations compared with the antenna 1 results. Figure 6(c) demonstrates the simulated results for antenna C in scenario 2 with its corresponding measurement results. Scenario 2 was much more complex compared to scenario 1, which caused more violent signal fluctuations.

In scenario 3, the two antennas transmit radio signals from the RUs sharing the same BTS. As a result, the measured data cannot distinguish the received signal with the transmitting antenna and a compound signal was obtained. In order to make a fair comparison, we also compounded the received signal from both antennas in the simulation. There is an NLOS area for both two transmitting antennas in this scenario, so an obvious signal loss can be found at the distance of 1400 m to 1800 m in Figure 6(d).

To statistically analyze all three simulation results with their corresponding experimental results, the RMSE and the mean absolute error (MAE) of the differences between the measurement results and prediction results are listed in Table 3. All analyses considered only the far-field results regardless of those near field values topped at -47 dBm. The simulation results obtained by the proposed method are consistent with the measurement data, with the RMSE around 4 dB and the MAE around 3 dB. Comparing the results with the existing published works for high-speed railway ray tracing applications based on DEM maps or manual 3D models, which obtained the simulation with RMSE at

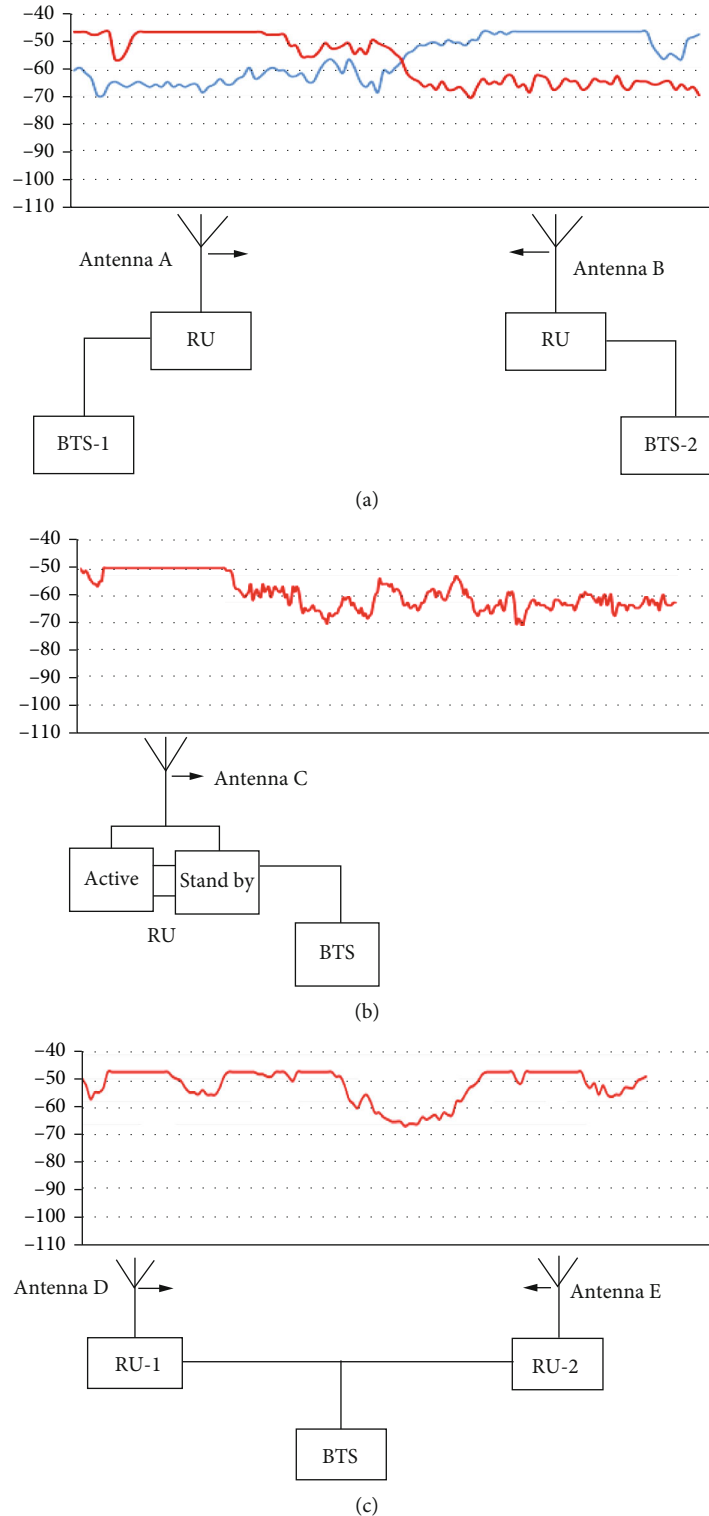
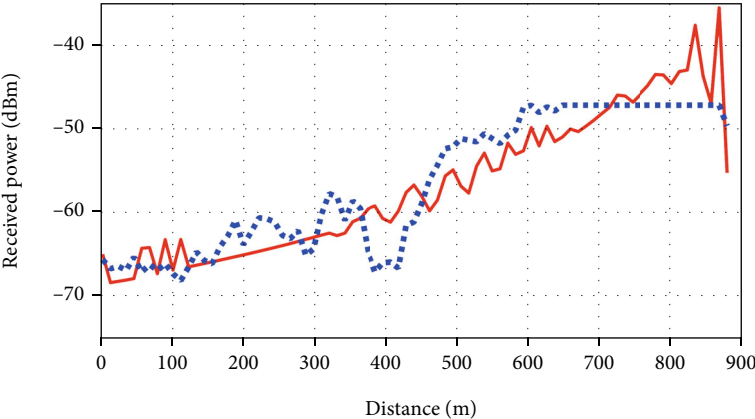


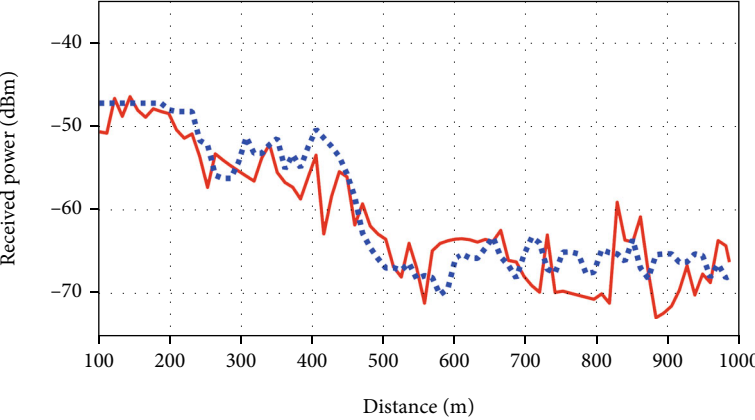
FIGURE 5: Field experiment results in contrast to the wireless system design. BTS: base transceiver station; RU: remote unit. (a) Antenna A and antenna B in scenario 1. (b) Antenna C in scenario 2. (c) Antenna D and antenna E in scenario 3.

about 5 dB in viaduct areas [2] and MAE above 5 dB in railway tunnels [19], our proposed method implementing highly accurate 3D railway environment model promotes the accuracy of radio propagation prediction.

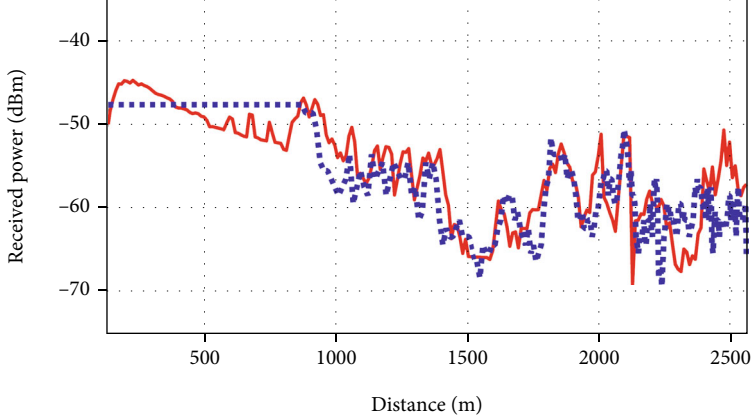
By analyzing the result, two main aspects may give rise to RMSE and MAE. The first aspect lies in the ray tracing method. Since ray tracing predicts the received power under ideal conditions, regardless of other external factors, such as



(a)

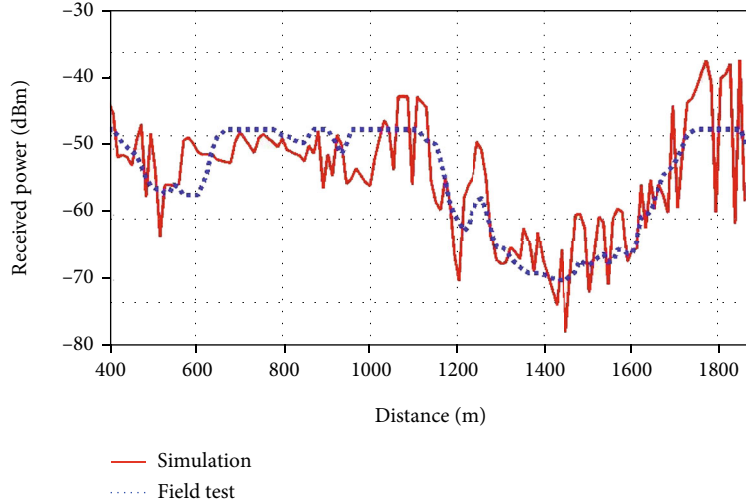


(b)



(c)

FIGURE 6: Continued.



(d)

FIGURE 6: RSSI comparison between the simulation results and the experimental results for (a) curve A for antenna A in scenario 1, (b) curve B for antenna B in scenario 1, (c) curve C for antenna C in scenario 2, (d) curve D for the composed signal from both antennas D and E in scenario 3.

TABLE 3: The RMSE and MAE of the difference between the measurements and predictions.

	RMSE (dB)	MAE (dB)
Curve A	3.41	2.91
Curve B	3.79	3.16
Curve C	4.14	3.31
Curve D	4.76	4.05

the influence of humidity on vegetation and soil. In our proposed method, we regard all soil material and vegetation material as uniformed materials. However, according to ref. [31], the humidity is highly relevant to the relative permittivity of the material, especially for soil. So the inaccuracy in material parameters causes inaccurate predictions. On the other hand, the second aspect affecting the predicted RMSE lies in the environment model. The real-world open-area environment is not static. Since the model acquirement and the experiment was not simultaneously conducted, the environmental changes may make the 3D environment model different from reality when conducting field test in the environment. To further improve the accuracy of ray tracing simulations, an accurate relative permittivity extraction method together with a timely updated 3D environment model is needed.

3.3. Model Lightweighting and Computational Complexity.

OAP 3D environment models consist of large amounts of data, which massively adds to the ray tracing computational complexity. The problem is particularly serious when dealing with higher-order field components. Therefore, the environment model should be light-weighted before implementing in the ray tracing simulator.

To evaluate the model lightweighting, we first governed the computational complexity of the ray tracing algorithm. The ray tracing simulator calculates the RSSI of the propaga-

tion paths in two steps. Firstly, the paths from the transmitting to the receiving antennas were literally traced. Then the attenuation suffered by the obstacles in each path was calculated. For large-scale ray tracing applications implementing the IM scheme, every facet or edge in the environment model should be tested. However, only a small amount of the environment model elements actually react to the ray propagation processes. As a result, most of the computational complexity lies in pathfinding rather than path loss calculations. We analyzed the computational complexity for each multipath component by multiplying the number of observation points with their corresponding interacting environment model elements. Assuming that the computational complexities in finding all subpaths are the same as calculating the direct ray, all results refer to the computational complexity of a single direct path as the reference unit (U_{LOS}). The computational complexities for each reflected and diffracted component were calculated using

$$\frac{C_{R_i}}{U_{LOS}} = N_p N_f (N_f - 1)^{i-1}, \quad (3)$$

$$\frac{C_{D_i}}{U_{LOS}} = N_p N_e (N_e - 1)^{i-1}, \quad (4)$$

where C_{R_i} and C_{D_i} are the computational complexity for the i -th order reflected and diffracted field components, respectively, N_p is the number of observation points along the railway track, N_f is the total number of triangular facets, and N_e is the total number of edges in the environment model. The computational complexity for the direct field (C_{Direct}) and transmitted field (C_{Trans}) are both equal to N_p since no extra steps should be taken when finding the propagation paths. The calculation results are demonstrated in Table 4. The statistical analysis shows that the

TABLE 4: Statistical analyses of the computational complexity for each multipath component.

	Scenario 1		Scenario 2		Scenario 3	
	OAP model	Light-weighted model	OAP model	Light-weighted model	OAP model	Light-weighted model
N_f	1.14×10^7	2.03×10^4	7.43×10^7	8.43×10^4	4.56×10^7	5.3×10^4
N_e	1.86×10^7	3.31×10^4	1.16×10^8	1.31×10^5	6.79×10^7	7.89×10^4
N_p	1018	1018	2608	2608	2363	2363
Direct field (C_{Direct})	1018	1018	2608	2608	2363	2363
Transmitted field (C_{Trans})	1018	1018	2608	2608	2363	2363
1st-order reflected field (C_{R_1})	1.16×10^{10}	2.07×10^7	1.94×10^{11}	2.20×10^8	1.08×10^{11}	1.25×10^8
2nd-order reflected field (C_{R_2})	1.33×10^{17}	4.20×10^{11}	1.44×10^{19}	1.85×10^{13}	4.91×10^{18}	6.63×10^{12}
1st-order diffracted field (C_{D_1})	1.89×10^{10}	3.37×10^7	3.02×10^{11}	3.42×10^8	1.6×10^{11}	1.86×10^8
2nd-order diffracted field (C_{D_2})	3.52×10^{17}	1.12×10^{12}	3.50×10^{19}	4.49×10^{13}	1.09×10^{19}	1.47×10^{13}
Total	4.84×10^{17}	1.54×10^{12}	4.94×10^{19}	6.34×10^{13}	1.58×10^{19}	2.13×10^{13}

Computational complexity (U_{Los})

TABLE 5: The proportions of summed RSSI for each multipath component in the three simulation results.

	Scenario 1		Scenario 2	Scenario 3	
	Antenna A	Antenna B	Antenna C	Antenna D	Antenna E
NLOS coverage rate	0%	0.79%	35.89%	61.29%	78.98%
Direct field	88.65%	92.41%	38.35%	67.23%	29.27%
Transmitted field	0%	0%	0.02%	16.96%	1.07%
Reflected field					
1st order	11.35%	6.27%	0.44%	15.77%	14.16%
2nd order	0%	0%	0.001%	0.01%	0%
Diffraction field					
1st order	0%	1.32%	61.16%	0.03%	55.5%
2nd order	0%	0%	0.04%	0%	0%

computational complexity increased exponentially when computing higher-order reflection and diffraction components. The results also indicate that the light-weighted model saved over 99.99% of the computational complexity while obtaining highly accurate prediction results.

Although the proposed method largely reduces the data volume and promotes calculation efficiency, the implementation of OAP still puts limits on the processed data volume in the light-weighted environment models. OAP established environment models out of a large number of aerial photographs, which described the natural terrain with lower efficiency than the regular artificial constructions. Especially when dealing with vegetated areas, the bushes with leaves often made the 3D models distorted with overlapped triangular facets. For most ray tracing algorithms, vegetated areas are often regarded as simplified 3D surface models with a given empirical parameter that considers the influence of the vegetation [33]. As a result, methods should be taken to the model to extremely simplify those areas before the ray tracing calculations. In this paper, we used the 3D modeling software to manage the model lightweighting and applied higher levels of lightweighting for the natural terrain. However, over-simplification of the environment models led to severe model distortions, which lowered the accuracy of the simulations. Especially when the signal propagation was obstructed by vegetated natural terrain, the model distortion and breaking points led to severe errors in calculating diffracted field components. In order to avoid serious simulation degradation, the natural terrain model was described using excessive triangular facets than necessary after the lightweighting. That was the reason the light-weighted model still contains over 0.1% of the model vertices to describe the above-mentioned scenarios.

Compounding different modeling techniques to establish the environment model and choosing a more efficient way to express the natural terrain is a promising way to solve the problem and accelerate the ray tracing process one step further. For example, we can implement OAP to describe the artificial constructions and LiDAR to describe the natural terrain. Such compounding techniques take advantage of different reconnaissance technologies and further lightweight the environment model for ray tracing usage.

TABLE 6: The MSE and MAE comparison of the results including and excluding the 2nd-order components.

		RMSE (dB)	MAE (dB)
Curve A	2nd order included	3.41	2.91
	2nd order excluded	3.41	2.91
Curve B	2nd order included	3.79	3.16
	2nd order excluded	3.79	3.16
Curve C	2nd order included	4.14	3.31
	2nd order excluded	4.15	3.34
Curve D	2nd order included	4.76	4.05
	2nd order excluded	4.75	4.04

3.4. Ray Tracing Strategy. Outdoor railway scenarios are often open-air applications with the transmitting antenna above the roof of trains. In our selected railway scenarios, the observation points along the railway tracks in scenarios 1 and 2 are mostly in good line-of-sight (LOS) with the signal towers. As a result, higher-order multipath components seldom appear, and propagation predictions considering merely low-order multipath components should achieve fairly high accuracy. Scenario 3 is a NLOS dominating area. In such areas, natural terrain structures are usually large in size, which makes the higher-order diffractions experience large path loss comparing with the low-order components. As a result, high-order multipath components do not contribute much to the RSSI results in railway scenarios. Therefore, it is a straightforward way to ignore the second-order calculations and accelerate the ray tracing algorithm with slightly compromised prediction accuracy.

To support the above-mentioned ray tracing strategy, we summed the absolute value of the RSSIs for each separated path with their corresponding multipath components in all observation points, the results of all three simulation processes are demonstrated in Table 5. Antenna A and antenna B were in scenario 1, which was a LOS dominating scenario. According to the statistical analysis results, the direct field and the first-order reflected field consisted of most of the received signal. In this scenario, the first-order diffraction

only occurred occasionally and the second-order components did not exist. Meanwhile, the situation for antenna C (Scenario 2) was much more complex. Since there were many non-line-of-sight observation points, the proportion of the transmitted and diffracted field components increased dramatically with appearing second-order components. However, the second-order components added together contributed to 0.04% of the total received signal. Scenario 3 is a special case for railways. The overall scenario is still an open area, which is similar to Scenario 1. However, the high-speed railway track experienced a curved line amount the valley, which resulted in a high NLOS coverage rate for wireless communication since the LOS transmission for the wireless signal was blocked by the surrounding environment to a great extent. According to the result, 61.29% and 78.98% of the wireless signal LOS transmission was blocked, respectively, for the two antennas in this scenario, and the two antennas showed different multipath component distributions. Antenna D was located close to the railway track, so the summed directed field was strong even under the circumstances that most areas in this scenario were NLOS areas. In this situation, the transmitted field, as well as the first-order reflected field, dominated the NLOS areas. In the meantime, antenna E shows a different situation. When the antenna is distant from the railway track, most NLOS areas were covered with the diffracted field.

Judging from all the above results, the sum of the direct, transmitted, first-order reflected, and first-order diffracted field components account for over 99% of the total received signal in this railway scenario. Furthermore, the MSE and MAE comparison results for all radio coverages when included and excluded the second-order components in the simulations are demonstrated in Table 6. The errors for all curves shows only slightly differences when excluding the 2nd-order calculations, indicating that implementing low-order multipath components in ray tracing can still accurately describe the radio propagation in the selected railway scenarios.

4. Conclusions

In this paper, we proposed a method to implement highly accurate 3D railway environment models on the ray tracing simulator and make radio propagation predictions along the railways. To adapt the 3D environment model to the ray tracing algorithm, we decomposed the environment models obtained by OAP into submodels for artificial construction and natural terrain, respectively. Different simplification levels were implemented on different submodels to lightweight environment models before they were imported to the ray tracing simulator. Simulations and real-world experiments were conducted to test the proposed method. The results show that a 4 dB RMSE in the selected railway scenarios was achieved with comparably low computational complexity. It was also found that the low-order multipath components account for most of the received radio signals in the selected railway scenarios. By focusing ray tracing on those low-order components regardless of the high-order ones, the algorithm can be further accelerated.

Data Availability

The datasets used to support the findings of this study are available from the corresponding author upon request.

Conflicts of Interest

The authors declare that there is no conflict of interest regarding the publication of this paper.

Acknowledgments

This research was funded by China Railway Siyuan Survey and Design Group Co. Ltd. (2020K183).

References

- [1] Z. Zhong, B. Ai, G. Zhu et al., *Dedicated mobile communications for high-speed railway*, Springer, 2018.
- [2] K. Guan, Z. Zhong, B. Ai, and T. Kurner, "Deterministic propagation modeling for the realistic high-speed railway environment," in *2013 IEEE 77th Vehicular Technology Conference (VTC Spring)*, pp. 1–5, Dresden, Germany, 2013.
- [3] J. Ding, L. Zhang, J. Yang, B. Sun, and J. Huang, "Broadband wireless channel in composite high-speed railway scenario: measurements, simulation, and analysis," *Wireless Communications and Mobile Computing*, vol. 2017, 15 pages, 2017.
- [4] M. Hatay, "Empirical formula for propagation loss in land mobile radio services," *IEEE Transactions on Vehicular Technology*, vol. 29, no. 3, pp. 317–325, 1980.
- [5] Y. Okumura, "Field strength and its variability in VHF and UHF land-mobile service," *Review of the Electrical Communication Laboratory*, vol. 16, pp. 825–873, 1968.
- [6] K. V. S. Hari, D. S. Baum, A. J. Rustako, R. S. Roman, and D. Trinkwon, "Channel models for fixed wireless applications," IEEE 802.16 Broadband wireless access working group, 2003.
- [7] A. Cost, "231, Digital mobile radio towards future generation systems. Final report," Tech. Rep. European Communities, EUR 18957, 1999.
- [8] C. Temaneh-Nyah and J. Nepembe, "Determination of a suitable correction factor to a radio propagation model for cellular wireless network analysis," in *5th International Conference on Intelligent Systems, Modelling and Simulation*, pp. 175–182, Langkawi, Malaysia, 2014.
- [9] N. Cota, A. Serrador, P. Vieira, A. R. Beire, and A. Rodrigues, "On the use of Okumura-Hat a propagation model on railway communications," in *16th International Symposium on Wireless Personal Multimedia Communications (WPMC)*, pp. 1–5, Atlantic City, NJ, USA, 2013.
- [10] A. Roivainen, P. Kyoesti, V. Hovinen, and C. F. Dias, "Validation of deterministic radio channel model by 10 GHz microcell measurements," in *European Wireless 2016; 22th European Wireless Conference*, pp. 1–6, Oulu, Finland, 2016.
- [11] A. Awada, A. Lobinger, A. Enqvist, A. Talukdar, and I. Viering, "A simplified deterministic channel model for user mobility investigations in 5G networks," *2017 IEEE International Conference on Communications (ICC)*, 2017, pp. 1–7, Paris, France, 2017.

- [12] Z. Yun and M. F. Iskander, "Ray tracing for radio propagation modeling: principles and applications," *IEEE Access*, vol. 3, pp. 1089–1100, 2015.
- [13] J. Nuckelt, M. Schack, and T. Kürner, "Deterministic and stochastic channel models implemented in a physical layer simulator for car-to-x communications," *Advances in Radio Science*, vol. 9, pp. 165–171, 2011.
- [14] A. Corucci, P. Usai, A. Monorchio, and G. Manara, *Wireless Propagation Modeling by Using Ray-Tracing*, Springer, New York, 2014.
- [15] D. He, B. Ai, K. Guan, L. Wang, Z. Zhong, and T. Kurner, "The design and applications of high-performance ray-tracing simulation platform for 5G and beyond wireless communications: a tutorial," *IEEE Communications Surveys & Tutorials*, vol. 21, no. 1, pp. 10–27, 2019.
- [16] K. Guan, Z. Zhong, B. Ai, R. He, and C. Briso-Rodriguez, "Five-zone propagation model for large-size vehicles inside tunnels," *Progress In Electromagnetics Research*, vol. 138, pp. 389–405, 2013.
- [17] K. Guan, Z. Zhong, B. Ai, and T. Kuerner, "Semi-deterministic path-loss modeling for viaduct and cutting scenarios of high-speed railway," *IEEE Antennas and Wireless Propagation Letters*, vol. 12, pp. 789–792, 2013.
- [18] K. Guan, Z. Zhong, B. Ai, and T. Kuerner, "Propagation measurements and modeling of crossing bridges on high-speed railway at 930 MHz," *IEEE Transactions on Vehicular Technology*, vol. 63, no. 2, pp. 502–517, 2014.
- [19] N. Sood, S. Baroudi, X. Zhang, J. Liebeherr, and C. D. Sarris, "Integrating physics-based wireless propagation models and network protocol design for train communication systems," *IEEE Transactions on Antennas and Propagation*, vol. 66, no. 12, pp. 6635–6645, 2018.
- [20] R. Rose and L. R. Basher, "Measurement of river bank and cliff erosion from sequential LIDAR and historical aerial photography," *Geomorphology*, vol. 126, no. 1–2, pp. 132–147, 2011.
- [21] F. Nex and F. Remondino, "UAV for 3D mapping applications: a review," *Applied Geomatics*, vol. 6, no. 1, pp. 1–15, 2014.
- [22] G. Yalcin and O. Selcuk, "3D city modelling with oblique photogrammetry method," *Procedia Technology*, vol. 19, pp. 424–431, 2015.
- [23] J. Cai, J. Chen, J. Li, and H. Peng, "Research on oblique aerial photography and its application in detection of hidden geological hazards," in *IOP Conference Series: Earth and Environmental Science*, p. 012124, Zhangjiajie, China, 2021.
- [24] L. Ling, "Research and application of Leica RCD30 oblique photogrammetric technology in urban 3D modeling (In Chinese)," *Henan Science and Technology*, vol. 20, pp. 16–17, 2018.
- [25] Z. Ming and W. Dong, "Application of A3 digital aerial photography system in aerial photography," *Urban Geotechnical Investigation & Surveying*, 2017.
- [26] Z. Yun and M. F. Iskander, "Radio propagation modeling and simulation using ray tracing," *The world of applied electromagnetics*, pp. 275–299, 2018.
- [27] H. Ling, R. Chou, and S. Lee, "Shooting and bouncing rays: calculating the RCS of an arbitrarily shaped cavity," *IEEE Transactions on Antennas and Propagation*, vol. 37, no. 2, pp. 194–205, 1989.
- [28] Z. Ji, B. Li, H. Wang, H. Y. Chen, and T. K. Sarkar, "Efficient ray-tracing methods for propagation prediction for indoor wireless communications," *IEEE Antennas and Propagation Magazine*, vol. 43, no. 2, pp. 41–49, 2001.
- [29] J. Li, L. Liu, and K. Guan, "Oblique aerial photography high-resolution environment models for high-speed railway ray-tracing simulations," in *2021 IEEE 4th International Conference on Electronic Information and Communication Technology (ICEICT)*, pp. 549–552, Xi'an, China, 2021.
- [30] ITU, "Effects of building materials and structures on radio-wave propagation above about 100 MHz," *Recommendation (ITU-Report)*, pp. 1–32, 2021.
- [31] ITU, "Electrical characteristics of the surface of the earth," *Recommendation (ITU-Report)*, pp. 1–24, 2019.
- [32] 3GPP, "3GPP TS 05.08 Radio subsystem link control," *3GPP Technical Specification*, vol. 5, pp. 1–100, 2005.
- [33] K. L. Chee, J. Baumgarten, A. Hecker et al., "Propagation prediction and measurement in vegetated moderately built-up areas," in *European Conference on Antennas & Propagation IEEE*, pp. 3361–3365, Prague Czech Republic, 2012.